

Testing gravity on large scales by combining weak lensing with galaxy clustering using CFHTLenS and BOSS CMASS

Shadab Alam^{1,2,3} ^{*}, Hironao Miyatake^{4,5,6}, Surhud More⁵, Shirley Ho^{1,2}, Rachel Mandelbaum^{1,2}

¹ *Department of Physics, Carnegie Mellon University, 5000 Forbes Ave., Pittsburgh, PA 15213*

² *McWilliams Center for Cosmology, Carnegie Mellon University, 5000 Forbes Ave., Pittsburgh, PA 15213*

³ *Institute for Astronomy, University of Edinburgh, Royal Observatory, Blackford Hill, Edinburgh, EH9 3HJ, UK*

⁴ *Jet Propulsion Laboratory, California Institute of Technology, Pasadena, CA 91109*

⁵ *Kavli Institute for the Physics and Mathematics of the Universe (WPI), UTIAS, The University of Tokyo, Chiba, 277-8583, Japan*

⁶ *Department of Astrophysical Sciences, Princeton University, Peyton Hall, Princeton NJ 08544, USA*

13 December 2016

ABSTRACT

We measure a combination of gravitational lensing, galaxy clustering, and redshift-space distortions called E_G . The quantity E_G probes both parts of metric potential and is insensitive to galaxy bias and σ_8 . These properties make it an attractive statistic to test Λ CDM, General Relativity and its alternate theories. We have combined CMASS DR11 with CFHTLenS and recent measurements of β from RSD analysis, and find $E_G(z = 0.57) = 0.42 \pm 0.056$, an 13% measurement in agreement with the prediction of general relativity $E_G(z = 0.57) = 0.396 \pm 0.011$ using the Planck 2015 cosmological parameters. We have corrected our measurement for various observational and theoretical systematics. Our measurement is consistent with the first measurement of E_G using CMB lensing in place of galaxy lensing (Pullen et al. 2016) at small scales, but shows 2.8σ tension when compared with their final results including large scales. This analysis with future surveys will provide improved statistical error and better control over systematics to test General Relativity and its alternate theories.

Key words: gravitation; modified gravity; galaxies: statistics; cosmological parameters; large-scale structure of Universe

1 INTRODUCTION

The theory of General Relativity (GR) is the most successful theory of the gravity. The GR was first proposed by Einstein (1915). GR has passed the most stringent tests at solar system scales (Sakstein 2015). But it is still an ongoing pursuit to test the predictions of GR at cosmological scale before we finally declare that it is the ultimate theory of gravity. There are some observational mysteries like dark matter (Zwicky 1937; Kahn & Woltjer 1959; Rubin & Ford 1970) and dark energy (Riess et al. 1998; Perlmutter et al. 1999) which cannot be explained with the current models. But if one ignores the questions about origin of dark matter and dark energy, then Λ CDM-GR is in good agreement with Cosmic Microwave Background (CMB) (Bennett et al. 2013; Planck Collaboration et al. 2014a), Baryon Acoustic Oscillation (BAO) (Eisenstein et al. 2005; Cole et al. 2005; Hütsi 2006; Kazin et al. 2010; Percival et al. 2010; Anderson et al. 2014a,b) and Hubble constant (Riess et al. 2011). One of the fundamental theoretical mysteries is the incompatible nature of quantum mechanics and GR. The nature of time in the two theories is so different that it is difficult to combine them in a

single framework (Unruh 1993; Anderson 2010). In order to further the understanding of these mysteries and develop consistent theories, it is important to test the predictions of these theories in various regimes. A fundamental difficulty of testing modifications to GR is the ability to absorb these modifications in dark energy. Fortunately, modified gravity predicts large scale structures different from those predicted by Einstein’s theory of gravity (Koyama 2006).

GR predicts many signatures of structure formation which can be observed in a wide variety of surveys. Two complimentary signals measured are weak gravitational lensing and redshift space distortions (RSD). Gravitational lensing was first proposed by Einstein in Einstein (1916). Weak gravitational lensing is a statistical measurement of deflection of photons due to gravitational interaction with the matter density (for a review, see Bartelmann & Schneider 2001; Refregier 2003; Schneider 2005; Hoekstra & Jain 2008; Massey et al. 2010; Weinberg et al. 2013). Its signal is imprinted in the cross-correlation of background galaxy shapes with foreground galaxy positions (e.g., Leauthaud et al. 2012; Mandelbaum et al. 2013; Velander et al. 2014; Han et al. 2015; Hudson et al. 2015; Zu & Mandelbaum 2015), and can be measured as “cosmic shear” (the auto- and cross-correlation of pairs of galaxy shapes;

^{*} email: salam@roe.ac.uk

e.g., Heymans et al. 2013; Jee et al. 2013). The redshift space distortion is the measurement of anisotropy produced in the galaxy auto-correlation function due to the peculiar velocity component in the galaxy redshift. This anisotropy allows us to measure the growth rate ($f = d \ln D / d \ln a$) of cosmic structure formation. It was first introduced by Kaiser (1987) and then further developed by others (Hamilton 1992; Scoccimarro 2004). It has been measured by various galaxy redshift surveys using different modeling schemes (Percival et al. 2004; Blake et al. 2011; Beutler et al. 2012; de la Torre et al. 2013; Chuang et al. 2016; Sánchez et al. 2013; Beutler et al. 2014; Alam et al. 2015b).

The larger surveys and novel combinations of probes will test the predictions of GR with unprecedented precision. One such combination of redshift space distortion and weak gravitational lensing was proposed by Zhang et al. (2007). It is important to test the relative amplitude of the effect of RSD and weak gravitational lensing as it probes space and time both parts of the metric. They have constructed a quantity E_G which can be measured by combining the signal from these two complimentary measurements. It has been proposed that E_G has the potential to serve as the most precise signal to test the nature of gravity (Zhang et al. 2007). E_G is independent of linear bias and the amplitude of matter fluctuations (σ_8). Reyes et al. (2010) has measured the first signal of E_G using a lower redshift sample from the Sloan Digital Sky Survey at an effective redshift of 0.32. Recently Blake et al. (2016) reported the measurement of E_G at two different redshifts, 0.32 and 0.57. A number of possible theoretical systematics of E_G is discussed in Leonard et al. (2015).

In this paper we measure E_G by combining the measurement of the weak gravitational lensing (Miyatake et al. 2015) from the Canada-France-Hawaii Lensing Survey (Heymans et al. 2012), hereafter referred to as CFHTLenS, with the measurement of redshift-space galaxy clustering from the Data Release 11 (DR11) CMASS sample (Alam et al. 2015a) of Baryon Oscillation Spectroscopic Survey (BOSS; Ahn et al. 2012), which is part of Sloan Digital Sky Survey III (SDSS-III; Eisenstein et al. 2011).

We have organized this paper in the following manner. In section 2, we provide some brief theoretical background of the E_G . Section 3 describes the samples of data used in our measurements. Section 4 describes the measurement of different components of E_G in detail with some systematic corrections. Section 5 provides the details of N -body simulation used in our analysis. The list of possible systematics affecting our E_G measurement with possible corrections is discussed in section 6. Finally, we provide our main measurement and estimate of uncertainty on the measurement in section 7. We end our paper with the discussion of the main points of our analysis and the implications of our results, along with some future directions, in section 8. Our fiducial cosmology is flat Λ CDM with $\Omega_m = 0.31$ and $h = 0.67$ all throughout the paper unless mentioned otherwise.

2 THEORY

The combination of galaxy-galaxy clustering, redshift space distortions and galaxy-galaxy lensing provides E_G . The measurements of lensing and clustering signals have been transformed to new quantities called Υ in order to reduce the impact of theoretical uncertainties and failures of certain approximations on small

scales (as discussed later). The combined probe E_G has been operationally defined in Reyes et al. (2010) as follows:

$$E_G(r_p) = \frac{\Upsilon_{gm}(r_p)}{\beta \Upsilon_{gg}(r_p)} \quad (1)$$

where $\beta = f/b$ is the redshift space distortion parameter with f being logarithmic derivative of growth with respect to scale factor and b is the linear bias. The quantities Υ_{gm} and Υ_{gg} are called galaxy-matter and galaxy-galaxy annular differential surface densities respectively (ADSDs; Baldauf et al. 2010). Υ_{gm} is defined as

$$\begin{aligned} \Upsilon_{gm}(r_p) &= \Delta \Sigma_{gm}(r_p) - \left(\frac{R_0}{r_p} \right)^2 \Delta \Sigma_{gm}(R_0) \\ &= \frac{2}{r_p^2} \int_{R_0}^{r_p} dR' R' \Sigma_{gm}(R') - \Sigma_{gm}(r_p) + \left(\frac{R_0}{r_p} \right)^2 \Sigma_{gm}(R_0). \end{aligned} \quad (2)$$

The observable for the weak gravitational lensing is the sum of the tangential shear from lensing (γ_t^G) and galaxy intrinsic shear (γ^I). Assuming galaxy intrinsic shear is negligible, lensing observation is proportional to $\Delta \Sigma(r_p) = \bar{\Sigma}(< r_p) - \Sigma(r_p)$, which is a measure of excess surface mass density. The value of $\Delta \Sigma(r_p)$ depends on all scales below r_p , which is not quite well described by linear theory. Υ_{gm} , shown in Eq. (2), is an attempt to cast the lensing observable $\Delta \Sigma(r_p)$ in such a way that it becomes independent of information below a certain scale R_0 . Υ_{gg} is defined as

$$\Upsilon_{gg}(r_p) = \rho_{crit} \left[\frac{2}{r_p^2} \int_{R_0}^{r_p} dR' R' w_{gg}(R') - w_{gg}(r_p) + \left(\frac{R_0}{r_p} \right)^2 w_{gg}(R_0) \right] \quad (3)$$

Here w_{gg} represents the projected galaxy-galaxy correlation function. These definitions ensure that despite measuring slightly different observables for the lensing and clustering, they are transformed to the same statistic of the correlation function, so that the theoretical prediction of E_G is equivalent to the measurement. Theoretically E_G can be defined in terms of metric perturbations:

$$E_G = \frac{\nabla^2(\Psi(r) - \Phi(r))}{3H_0^2 a^{-1} \theta}, \quad (4)$$

where θ is the perturbation in matter velocity field, H_0 is the Hubble parameter today and a is the scale factor. The ψ and ϕ represent metric perturbations to the time and space components, respectively, assuming a Friedmann-Robertson-Walker (FRW) metric with a flat universe. The numerator $\nabla^2(\Psi(r) - \Phi(r))$ probes the lensing convergence and the θ in denominator probes the redshift space distortions. As shown in Hojjati et al. (2011), the time-time and momentum Einstein field equation in GR, under the assumption of negligible anisotropic stress and non-relativistic matter species, becomes the simple algebraic equation,

$$k^2 \Psi = -4\pi G a^2 \rho(a) \delta, \quad (5)$$

$$\Phi = -\Psi, \quad (6)$$

where ρ is the background matter density and δ is the matter density perturbation. In modified theories of gravity these relations are different, which requires two extra functions $\mu(k, a)$ and $\gamma(k, a)$ to account for departure from GR (Hojjati et al. 2011).

$$k^2 \Phi = -4\pi G a^2 \mu(k, a) \rho \Delta \quad (7)$$

$$\Phi = -\gamma(k, a) \Psi, \quad (8)$$

The perturbation equations in Ψ and Φ are in Fourier space which should be related to its real space counterpart $\Psi'(r) = \Psi(k)e^{-ikr}$, $\Phi'(r) = \Phi(k)e^{-ikr}$. This gives us the relation $\nabla^2(\Psi'(r) - \Phi'(r)) = -k^2(\Psi(k) - \Phi(k))$. We combine the perturbation equation and the definition of E_G with $\Omega_M(z=0) = \frac{8\pi G\rho_o}{3H_o^2}$, $\rho = \rho_o a^{-3}$ and $\theta = -f\delta$ to get our theoretical prediction of $E_G = -\Omega_M(z=0)\mu(k, a)(\gamma(k, a) + 1)/2f$. The $E_G = \Omega_M(z=0)/f$ can be recovered for GR by substituting $\mu = -1$ and $\gamma = 1$.

It is non-trivial to see the connection between our theoretical definition (Eq. 4) and the observational definition (Eq. 1). We provide a brief outline to make this connection a little bit easier. Please refer to Reyes et al. (2010) and Baldauf et al. (2010) for more details. The statistics Υ for galaxy-matter and galaxy-galaxy can be written in terms of their corresponding power spectrum as follows.

$$\Upsilon_{gg, gm}(r_p; R_0) = \rho_{\text{crit}} \int P_{gg, gm} W_{\Upsilon}(k; r_p, R_0) dk, \quad (9)$$

where $W_{\Upsilon}(k; r_p, R_0)$ is the window function for Υ given in equation 17 of Baldauf et al. (2010). We know that galaxy-matter power spectrum is proportional to the cross power of convergence ($\nabla^2(\Psi - \Phi)$) and galaxy. This implies that $P_{gm} \equiv \langle \nabla^2(\Psi - \Phi)\delta_g \rangle$. We also know that galaxy-galaxy power spectrum can be written as follows,

$$P_{gg} \equiv \langle \delta_g \delta_g \rangle = -\frac{1}{\beta} \langle \theta \delta_g \rangle \quad (10)$$

The first equivalence is the definition of the galaxy-galaxy power spectrum. The second equality results from the fact that for linear regime, matter conservation relates velocity perturbations (θ) to matter perturbations (δ) by $\theta = -f\delta$ and, linear bias model relates δ to δ_g by $\delta_g = b\delta$. Now, the ratio of Υ_{gm} and $\beta\Upsilon_{gg}$ gives the ratio of power spectrum, which will be proportional to $(\nabla^2(\Psi - \Phi)\delta_g)/\theta\delta_g$. Therefore our observational definition given by Eq. (1) is same as the theoretical definition given by Eq. (4).

3 DATA

We use the SDSS-III BOSS CMASS sample and shape measurements from CFHTLenS data to measure the galaxy-galaxy clustering, galaxy matter cross-correlation and redshift space distortions parameter. We describe the data sets used in our analysis in the following sections.

3.1 BOSS CMASS

We use data included in data release 11 (DR11; Alam et al. 2015a) of the Sloan Digital Sky Survey (SDSS; York et al. 2000). Together, SDSS I, II (Abazajian et al. 2009) and III (Eisenstein et al. 2011) used a drift-scanning mosaic CCD camera (Gunn et al. 1998) to image over one-third of the sky (14555 square degrees) in five photometric bandpasses (Fukugita et al. 1996; Smith et al. 2002; Doi et al. 2010) to a limiting magnitude of $r < 22.5$ using the dedicated 2.5-m Sloan Telescope (Gunn et al. 2006) located at the Apache Point Observatory in New Mexico. The imaging data were processed through a series of pipelines that perform astrometric calibration (Pier et al. 2003), photometric reduction (Lupton et al. 1999), and photometric calibration (Padmanabhan et al. 2008). All of the imaging was reprocessed as part of SDSS Data Release 8 (DR8; Aihara et al. 2011). BOSS (Dawson et al. 2013)

is designed to obtain spectra and redshifts for 1.35 million galaxies over a footprint covering 10,000 square degrees. These galaxies are selected from the SDSS DR8 imaging and are being observed together with 160,000 quasars and approximately 100,000 ancillary targets. The targets are assigned to tiles using a tiling algorithm that is adaptive to the density of targets on the sky (Blanton et al. 2003). Spectra are obtained using the double-armed BOSS spectrographs (Smeed et al. 2013). Each observation is performed in a series of 900-second exposures, integrating until a minimum signal-to-noise ratio is achieved for the faint galaxy targets. This ensures a homogeneous data set with a high redshift completeness of more than 97% over the full survey footprint. Redshifts are extracted from the spectra using the methods described in Bolton et al. (2012). A summary of the survey design appears in Eisenstein et al. (2011), and a full description is provided in Dawson et al. (2013).

We use the CMASS sample of galaxies (Bolton et al. 2012) from Data Release 11. The CMASS sample has 690,826 massive galaxies covering 8498 square degrees in the redshift range $0.43 < z < 0.70$, which correspond to an effective volume of 6 Gpc³.

3.2 CFHTLENS

For the galaxy-galaxy lensing measurements, we use the deeper and better quality imaging data from the Canada France Hawaii Telescope Legacy survey (CFHTLS). This data allows us to measure the tangential distortion of background galaxies around our sample of CMASS galaxies. We use the photometric reduction and image shape determinations in the publicly available CFHTLenS catalog¹. The quantities needed for each galaxy, namely its shear estimate, shear calibration factors, weight, and the posterior distribution of its photometric redshift distribution are provided in the catalog (Heymans et al. 2012; Erben et al. 2013; Miller et al. 2013; Hildebrandt et al. 2012). We use the same quality cuts on the data as were applied in Miyatake et al. (2015). Finally we note that the overlap between the CFHTLS and the DR11 BOSS fields is limited to an area of about 105 deg². The number of CMASS galaxies that lie within the CFHTLS footprint is 8899.

4 MEASUREMENTS

The quantity E_G is a combination of galaxy-galaxy annular differential surface density (Υ_{gg}), galaxy-matter annular differential surface density (Υ_{gm}) and the redshift space distortion parameter (β). In the following section we describe the procedure to obtain each of these signals.

4.1 Galaxy-Galaxy annular surface density (Υ_{gg})

The data from SDSS-III BOSS includes the three-dimensional positional information of CMASS galaxies, which enables us to perform a high signal-to-noise measurement of the projected correlation function, w_p , and the associated Galaxy-Galaxy annular surface density, Υ_{gg} . We account for a number of subtle selection effects in order to obtain a precise measurement of clustering (Ross et al. 2012). The spectroscopic target sample is obtained from the SDSS imaging observations after the application of a variety of colour and photometric selection cuts (Dawson et al. 2013; Reid

¹ <http://www.cfhtlens.org/astronomers/data-store>

et al. 2016). However, due to the limited number of fibers available, not all galaxies from this target sample can be allocated a fiber while performing spectroscopic observations to determine their redshifts. This could also happen if two targets are within $62''$ of each other and hence cannot be simultaneously observed due to the finite size of fibers. If such fiber-collided galaxies lie in a region of the sky which is visited multiple times (due to overlaps in the target tiling) then they may have redshift measurements. There are also instances where a galaxy is assigned to a fiber, but its redshift could not be obtained. Finally, there are also instances where it is difficult to perform star-galaxy separation, especially in fields with a high number density of stars. These effects have been quantified in the parent DR11 catalog of CMASS galaxies by assigning a weight to each galaxy such that

$$w_l = w_* w_{\text{see}} (w_{\text{noz}} + w_{\text{cp}} - 1), \quad (11)$$

where w_{noz} is the weight assigned to a galaxy if it is the nearest neighbour (in the plane of the sky) of a redshift failure galaxy, w_{cp} is similarly assigned to account for the nearest neighbours of fiber collided galaxies², and w_* and w_{see} accounts for the systematic relationship between the density of stars and seeing (respectively) with the density of BOSS target galaxies (for details, see Anderson et al. 2014b). The BOSS parent catalog contains an additional weight, w_{FKP} , for each galaxy which depends upon the number density of galaxies in the sample at its redshift (Feldman et al. 1994). The total weight for each galaxy that we use is given by

$$w_{\text{tot}} = w_l w_{\text{FKP}}. \quad (12)$$

We use catalogues of random points with the same angular and redshift selection as our galaxy subsample. These random catalogs consist of about 50 times more points than the number of galaxies in each of our subsamples. We assign each random point a weight of $N_{\text{gal}}/N_{\text{ran}}$ to account for this difference. In practice, we use the random catalogs provided with SDSS DR11 (Reid et al. 2016).

We measure the correlation function of galaxies, $\xi(r_p, \Pi)$, where r_p is the projected separation of galaxies, and Π , their line-of-sight separation, using the estimator proposed by Landy & Szalay (1993),

$$\xi(r_p, \Pi) = \frac{DD - 2DR + RR}{RR}. \quad (13)$$

Here, DD , RR and DR represent the number of appropriately weighted pairs of galaxies with a given separation (r_p, Π) , where both galaxies lie either in the galaxy catalog or the random catalog or one in each of the catalogs, respectively. The projected correlation function is obtained by integrating $\xi(r_p, \Pi)$ along the line of sight,

$$w_p(r_p) = 2 \int_0^{\Pi_{\text{max}}} \xi(r_p, \Pi) d\Pi, \quad (14)$$

where we adopt $\Pi_{\text{max}} = 100h^{-1}\text{Mpc}$. We then convert the projected correlation function into galaxy-galaxy annular differential surface density following Eq. (1), where we adopt $R_0 = 1.49h^{-1}\text{Mpc}$. Figure 4 shows the projected correlation function and galaxy-galaxy ADSDs measured from data and simulation. We

carry out this measurement at $1.2 < r_p < 47 h^{-1}\text{Mpc}$ divided into 9 bins.

4.2 Galaxy-Matter annular surface density (Υ_{gm})

For the weak lensing measurement, we followed the procedure described in Miyatake et al. (2015). In this paper we summarize the procedure; we encourage those who are interested in details to read reference. The tangential shear caused by lensing is related to the excess surface mass density as

$$\gamma_t^G = \frac{\Delta\Sigma(r_p)}{\Sigma_{\text{cr}}}, \quad (15)$$

where Σ_{cr} is defined as

$$\Sigma_{\text{cr}}(z_l, z_s) = \frac{c^2}{4\pi G} \frac{d_A(z_s)}{d_A(z_l)d_A(z_l, z_s)(1+z_l)^2}. \quad (16)$$

Here, $d_A(z_l)$, $d_A(z_s)$, and $d_A(z_l, z_s)$ are the angular diameter distance to lens, source and between lens and source. The factor of $(1+z_l)^{-2}$ is due to our use of comoving coordinates. Using lens-source pairs, the excess surface mass density is calculated as

$$\Delta\Sigma(r_p) = \frac{\sum_{ls} w_{ls} e_t^{ls} \Sigma_{\text{cr}}^{ls}}{(1 + K(r_p)) \sum_{ls} w_{ls}}, \quad (17)$$

where e_t is the ellipticity of a source galaxy given by the CFHTLenS catalog³. When calculating Σ_{cr}^{ls} , we use the probability distribution function of photometric redshift (photo- z). We use the weight $w_{ls} = w_{\text{tot},l} w_s \Sigma_{\text{cr}}^{-2}$, where $w_{\text{tot},l}$ is the weight of each lens galaxy given by Eq. (12) and w_s is the weight of each galaxy given by the CFHTLenS catalog. The factor of $(1 + K(r_p))^{-1}$ is calculated using the multiplicative bias correction factor given by the CFHTLenS catalog. We use the same r_p binning as the clustering measurement (Υ_{gg}).

We perform two systematic tests for the lensing measurement. The first is a test for contamination from galaxies that are physically associated with lens galaxies, and therefore not lensed. If we wrongly select those galaxies as sources, the lensing signal is diluted. This effect can be diagnosed using the so-called ‘‘boost factor’’ which is a ratio of the sum of the weight of galaxies behind lens galaxies to that behind random points (Sheldon et al. 2004). If the lensing signal is diluted, the boost factor is larger than unity. In our measurement, we find the boost factor is consistent with unity within 1.6% at $r_p \gtrsim 1.5 h^{-1}\text{Mpc}$, the scales used for this study. The statistical error in the boost factor is subdominant compared to the statistical error coming from the shape noise. The second systematic test is for the effect of imperfect PSF correction. This can be diagnosed by measuring the lensing signal around random points, which exhibits a spurious signal for certain types of imperfection in the PSF correction. In our measurement, the lensing signal around random points deviates from zero at $r_p \gtrsim 5 h^{-1}\text{Mpc}$. We find that the 45-degree rotated signal, which should be consistent with zero around galaxies, deviates from zero at these scales. After subtracting the signal around random points, the 45-degree rotated signal becomes consistent with zero except for the outermost bin at $r_p \sim 40 h^{-1}\text{Mpc}$. Thus we apply the same correction to the lensing signal, and discard the outermost bin. The correction ranges from 5% to 14% of the lensing signal before correction.

² Nearest neighbour corrections have been shown to accurately correct for fiber collisions above the fiber collision scale ($\sim 0.4h^{-1}\text{Mpc}$) by Guo et al. (2012). Both w_{noz} and w_{cp} are equal to unity by default for all galaxies. Their values are incremented for the nearest neighbours of every redshift failure or fiber collided galaxy.

³ The ellipticity in the CFHTLenS catalog is defined by $|e| = (a-b)/(a+b)$, where a and b are the semi-major and semi-minor axes of the ellipse. The ensemble expectation value of this ellipticity definition is equal to the lensing shear.

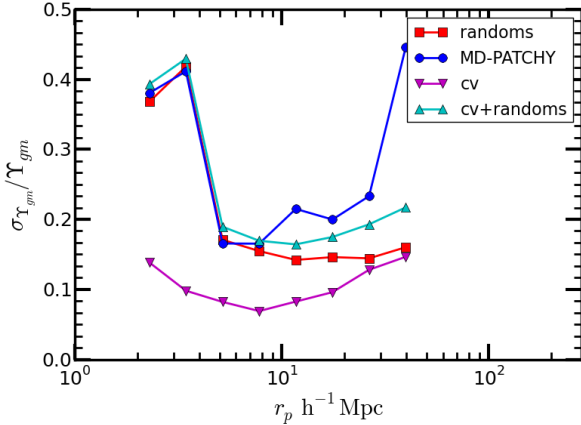


Figure 1. The plot shows the fractional error in galaxy-matter annular surface density (Υ_{gm}) as a function of r_p . The blue circles show the error estimate using MD-Patchy mocks, the red squares show the error estimates from random lenses, the magenta triangles are estimates of the cosmic variance contribution from N -body simulations, and the cyan triangles are obtained by adding cosmic variance and the error from random lenses in quadrature. We use the error estimate from MD-Patchy in our final results.

The statistical uncertainty on this correction is very small since the number of random points is much larger than the number of real lenses. This correction is a valid way to correct for shear systematics that were not fully removed by the PSF correction routine, provided that the source of the systematics does not correlate with the lens number density. Since the lenses are selected in one survey and the shears measured in another, there is no reason for such a correlation to exist, so the correction is valid and we do not associate a systematic uncertainty with this correction (Mandelbaum et al. 2005).

When calculating the covariance of the lensing signal, we must account for the correlated shape noise, lens shot noise, and cosmic variance. The correlated shape noise is caused by the use of the same source galaxies multiple times, since the stacking annuli overlap for different lens galaxies. The lens shot noise stems from the noise in the distribution of redshift or other properties of CMASS galaxies in the CFHTLenS field due to the small area compared to the full BOSS sample. The cosmic variance is due to the large-scale fluctuation modes larger than a survey region. To account for them, we estimate the covariance matrix using 150 realizations of the lensing signal around MD-Patchy mocks (Kitauro et al. 2016). We compare this covariance to that estimated from the lensing signal around random points, which is considered to have just part of the correlated shape noise⁴, and find that the lens shot noise and cosmic variance make up about the half of the covariance at $r_p \gtrsim 10 h^{-1} \text{Mpc}$. We also calculate the expected covariance by adding the random covariance to the lens shot noise and cosmic variance estimated from N -body simulations (see Section 6.6 for details). We confirm that the difference between the covariance estimated from MD-Patchy mocks and the expected covariance is within 3 per cent at $r_p \lesssim 30 h^{-1} \text{Mpc}$. Figure 1 shows a comparison of the lensing error estimates from different sources. We use the error estimate from MD-Patchy in our final results.

We then convert the excess surface mass density and its covariance into galaxy-matter annular differential surface density fol-

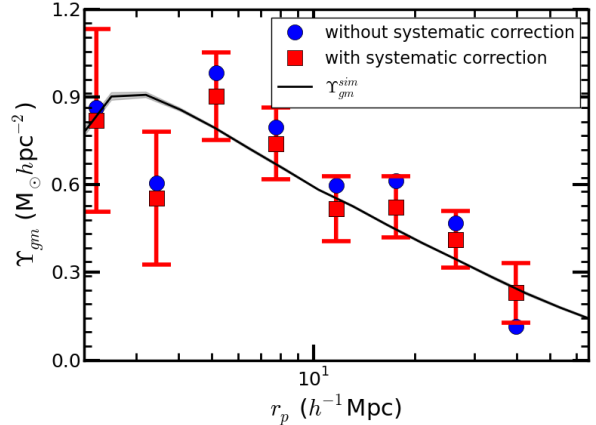


Figure 2. The plot shows the galaxy-matter annular surface density (Υ_{gm}) measured from CFHTLenS and CMASS catalogues. The blue points are measurements before and red points are after applying an additional systematic correction for imperfect PSF correction resulting in additive shear systematics. The black line and shaded region shows the measurement of Υ_{gm} and 1σ error from an N -body simulation.

lowing Eq. (2). Figure 2 shows our measured galaxy-matter annular differential surface density, including the size of the systematic correction for imperfect PSF correction.

4.3 Redshift Space Distortions parameter (β)

We measure the two-dimensional auto-correlation function of the BOSS CMASS galaxies using the Landy-Szalay (Landy & Szalay 1993) estimator. The correlation function is first binned in (r, μ) , where r is the three-dimensional galaxy pair separation and $\mu = \cos(\theta)$ with θ being the angle made by the pair of galaxies from the line of sight. The galaxy-galaxy auto-correlation is projected onto the Legendre basis in order to obtain the monopole (ξ_0) and quadrupole (ξ_2) moments. The monopole and quadrupole moments of the correlation function are evaluated between 6 to $198 h^{-1} \text{Mpc}$ in linear bins of width $8 h^{-1} \text{Mpc}$. The bin size of $8 h^{-1} \text{Mpc}$ is chosen to optimize signal-to-noise without smoothing out the important physics. We have used 600 PTHalo mocks (Manera et al. 2013) to generate an estimate of the covariance matrix for the measured correlation function. The fit to the monopole and quadrupole moments of the correlation function is obtained using Convolution Lagrangian Perturbation Theory (CLPT) and Gaussian Streaming Model (GSM) (Carlson et al. 2013; Wang et al. 2014).

The theoretical model has been tested using PTHalo mocks. It was shown that our model gives accurate prediction of $\xi_{0,2}$ at scales ranging from $30 h^{-1} \text{Mpc}$ to $126 h^{-1} \text{Mpc}$ with $8 h^{-1} \text{Mpc}$ bin width. The measured $f\sigma_8(z = 0.57) = 0.462 \pm 0.041$ and $b\sigma_8(z = 0.57) = 1.194 \pm 0.032$, as reported in Alam et al. (2015b). The RSD parameter β is computed by taking the ratio of the measured growth rate f and bias b , i.e., $\beta = f/b$. This gives us $\beta(z = 0.57) = 0.387 \pm 0.042$, while accounting for the correlation between growth rate and bias. The complete redshift space distortion analysis is reported in Alam et al. (2015b), including the list of parameters marginalized and prior used on those parameters in table 2 of that work. A comparison of this measurement with other similar measurements is shown in Figure 6 of Alam et al. (2015b).

⁴ Clustered lenses have more correlated shape noise than random points.

We note that the measurement of β is obtained using scales above $30 h^{-1}\text{Mpc}$ whereas our final E_G measurement use scales below $30 h^{-1}\text{Mpc}$. Ideally one would want to measure β using same scales. But, unfortunately, the modeling used in the current measurement of β is not good enough to extend to smaller scales. The β consists of two quantities, growth rate and bias. We do account for the fact that bias will be scale dependent and different at smaller scale compared to large scale measurement through a correction factor C_b (see section 6.1 for details). But we have an inherent assumption that the growth rate measured using larger scales are constant and applicable for smaller scales. This makes the current measurements of E_G slightly weaker than its full potential, which should be improved upon in the future measurements with better RSD modeling.

5 N-BODY SIMULATIONS

We use N -body simulations in order to investigate systematic effects and estimate various possible systematic corrections. We use an N -body simulation run using the TreePM method (Bagla 2002; White et al. 2002; Reid et al. 2014), provided by Martin White. We are using 10 realizations of this simulation based on the ΛCDM model with $\Omega_m = 0.292$ and $h = 0.69$. These simulations are in a periodic box of side length $1380 h^{-1}\text{Mpc}$ and 2048^3 particles. A friend-of-friend halo catalogue was constructed at effective redshift of $z = 0.55$. This is appropriate for our measurements since the galaxy sample used has effective redshift of 0.57. We have found weak redshift evolution of the clustering signal as shown in Figure 3. Therefore our simulations at mean redshift without any redshift evolution should provide a good approximation to the original data.

The Halo Occupation Distribution (HOD; Peacock & Smith 2000; Seljak 2000; Benson et al. 2000; White et al. 2001; Berlind & Weinberg 2002; Cooray & Sheth 2002) is used to relate the observed clustering of galaxies with halos measured in the N -body simulation. The HOD model used was proposed in White et al.

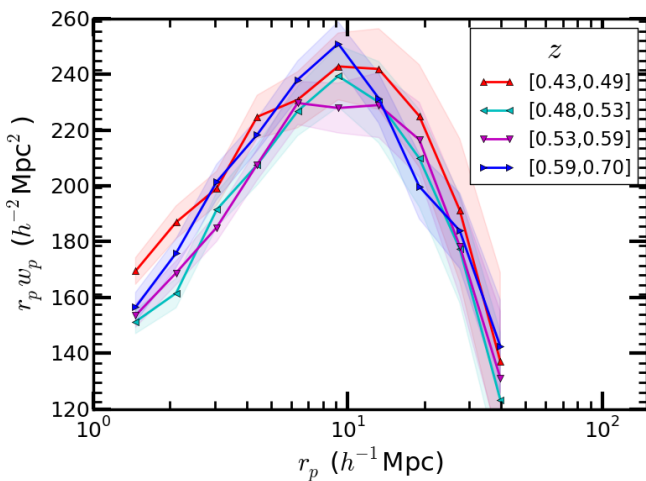


Figure 3. The CMASS sample is divided into four redshift bins, each containing roughly equal number of galaxies. We show the w_p for each of the redshift bins, with the shaded region showing the 1σ uncertainty estimated using the jackknife. We found weak redshift evolution and hence our simulation at fixed redshift should provide a good description of the sample despite its non-negligible redshift range.

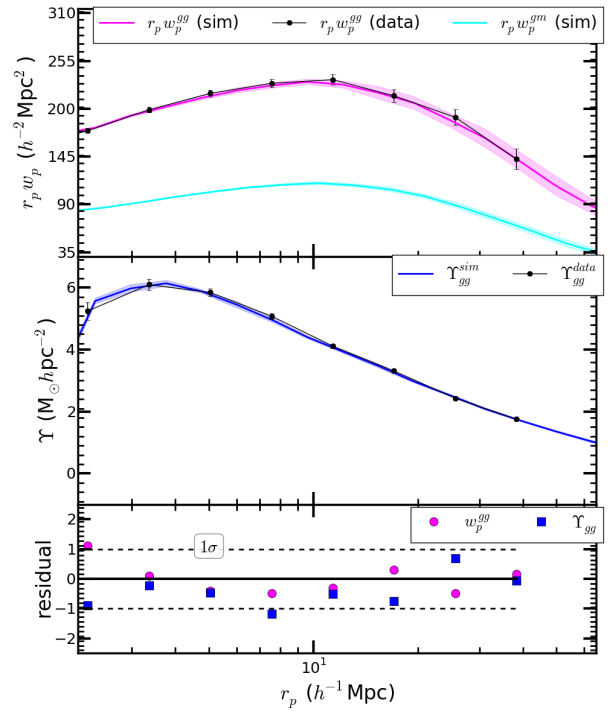


Figure 4. The top panel shows the projected correlation function, middle panel shows ADSDs and the bottom panel shows the residual between data and simulation as the function of r_p . The black dots are measurement from the BOSS CMASS sample. The red and blue line represents measurements of galaxy-galaxy and galaxy-matter clustering from N -body simulations. The shaded regions are standard deviation of 10 N -body simulations. The red and blue points in the bottom panel shows that the residuals (normalized by statistical uncertainties) are within 1σ for both w_p^{gg} and γ_{gg} respectively. This shows that our simulations and observations gives consistent results.

(2011) to populate the halo catalogue with galaxies. The number of galaxies hosted in each halo is a function of halo mass; halos can host central and satellite galaxies. The occupation distributions are

$$\begin{aligned} \langle N_{\text{cen}} \rangle_M &= \frac{1}{2} \text{erfc} \left(\frac{\ln(M_{\text{cut}}/M)}{\sqrt{2}\sigma} \right), \\ \langle N_{\text{sat}} \rangle_M &= \langle N_{\text{cen}} \rangle_M \left(\frac{M - \kappa M_{\text{cut}}}{M_1} \right)^\alpha, \end{aligned} \quad (18)$$

where $\langle N_{\text{cen}} \rangle_M$ is the average number of central galaxies for a given halo mass M and $\langle N_{\text{sat}} \rangle_M$ is the average number of satellites galaxies. The HOD parameters we used⁵ are ($M_{\text{cut}} = 1.77 \times 10^{13} M_\odot/h$, $M_1 = 1.51 \times 10^{14} M_\odot/h$, $\sigma = 0.897$, $\kappa =$

⁵ These HOD parameters were obtained by carrying out a fit to the projected clustering signal, w_p measured in Section 4.1, and the CMASS galaxy abundance using the analytical halo model framework (van den Bosch et al. 2013; More et al. 2013; Cacciato et al. 2013). The analytical halo model developed in these papers accounts for halo exclusion, radial dependence of halo bias, and the residual redshift space distortions due to finite extent of the line-of-sight integration used to compute w_p . We refer the reader to these papers and to More et al. (2015) for the details of the modelling procedure. Since the quoted HOD corresponds to halos with an overdensity of 200 with respect to the background, while the halos in simulations were obtained using the FOF algorithm, we used the relation between FOF halo masses and SO halo masses derived in More et al. (2013) for idealized Navarro-Frenk-White halos. While this correction is not per-

0.137, $\alpha = 1.151$). We have populated central galaxies at the center of the halos. The satellite galaxies are populated with radius (distance from the central galaxy) distributed as per the NFW profile out to r_{200} , and the direction is chosen randomly with a uniform distribution assuming satellites are spherically distributed. It is a good approximation because only $\sim 10\%$ of the galaxies are satellites. The central galaxies are each assigned the same velocity as their halo. The satellite galaxies are assigned velocities which are normally distributed, with mean as the halo velocity and dispersion the same as the halo velocity dispersion.

We find that the clustering measurement between our N -body simulation and measurement agrees within 1σ . The top panel of Figure 4 shows the projected galaxy-galaxy (red) and galaxy-matter (blue) correlation functions. The shaded regions are the standard deviation of 10 N -body mocks. The galaxy-galaxy projected correlation function measured from data shown in black points agrees quite well with the one measured from N -body simulation. The projected galaxy-galaxy correlation is used to measure Υ_{gg} , which is shown in the middle panel of Figure 4. The projected galaxy-matter cross-correlation function is used to compute Υ_{gm} , which is shown in Figure 2. The measurement of Υ_{gm} from the N -body simulation (using the w_p -based HOD parameters) and data agrees very well. We used this HOD populated galaxy sample to compute some of the systematic corrections on our measurement (see Section 6 for details). Such correction will have an error due to the uncertainty in HOD parameters. Since the HOD parameters are very well constrained due to small error on clustering measurements we expect such error to be small compared to the correction.

6 POTENTIAL SYSTEMATICS

We investigate various possible systematic effects which can affect our measurement of E_G . We will show that some of them are negligible and have computed corrections for others. These corrections are small compared to the statistical uncertainty on the measurement. We have applied these systematic corrections to our final measurement. An alternative approach to account for these systematic shifts is to apply them to the theoretical prediction as shown in Leonard et al. (2015).

6.1 Scale dependence of bias

Galaxies are formed in dark matter halos, which makes the clustering amplitude of galaxies biased compared to that of dark matter. The massive galaxies used in our analysis are a highly biased sample. It has been shown that a linear bias model fails to match the observations and simulations at small scales (Saito et al. 2014). E_G is constructed in such a way that it is independent of linear bias. However, the redshift space distortion parameter β is computed using the linear bias whereas the projected correlation function is calculated at smaller scales, where the bias is scale-dependent, the causing bias factor in E_G to not completely cancel. To correct for this factor, we compute the correction factor $C_b(r_p) = \Upsilon_{gg}(r_p)/b\Upsilon_{gm}(r_p)$ from mock catalogs in Section 5, as proposed by Reyes et al. (2010). The correction factor $C_b(r_p)$ is shown in Figure 5, where linear bias $b = 1.95$ was measured in RSD analysis of our N -body simulation using RSD

model of Alam et al. (2015b). The Υ_{gg} and Υ_{gm} for this correction is computed using 10 N -body simulations shown in Figure 4. The scale-dependent bias correction C_b has maximum value of 8% at $8 h^{-1}\text{Mpc}$. It is important to note that our scale-dependent bias correction does not approach 1 at the large scales used for this analysis, contrary to our expectations. This is because our largest scale is still in quasi-linear regime and hence the scale-dependent bias correction does not approach 1.

6.2 Difference in Lensing and Clustering Window

E_G includes the ratio of the galaxy-galaxy auto-correlation with galaxy-matter cross-correlation measured from lensing. The galaxy-galaxy auto-correlation is measured in redshift space with a top-hat window. The galaxy-matter cross-correlation, on the other hand, is measured with very broad lensing window that washes out the effect of redshift space distortions and behaves differently with line of sight separation compared to a top-hat. To correct both of these effects, we use the window function correction (C_{win}). The window function correction consists of two parts $C_{win} = C_{RSD}C_{integration}$, where the C_{RSD} is the ratio of Υ_{gg} in redshift and in real space. We compute this correction by evaluating the clustering in real and in redshift space from 10 N -body simulations.

The motivation for the $C_{integration}$ correction is as follows. When making our theoretical predictions for E_G , we begin from a 3D model that we assume is projected to 2D in the same way for both galaxy-galaxy and galaxy-matter correlations, using $\int_{-\Pi_{max}}^{\Pi_{max}} \xi_{gg,gm}(r_p, \pi) d\Pi$. This is a top-hat window with a hard cutoff at Π_{max} . However, reality provides us with a lensing shear signal that is projected using a non-top-hat window. It is not truncated at Π_{max} , and it is not flat like a top-hat. We must consider a more generalized situation with some window function $W(\Pi)$ using $\int_{-\Pi_{max}}^{\Pi_{max}} \xi_{gm}(r_p, \Pi) W(\Pi) d\Pi$. Thus, the ratio of quantities used to construct E_G should differ slightly from the theory prediction that assumes a top-hat window for both. The correction factor by which we should multiply our observed E_G (before comparing with theory) is $C_{integration}$, the ratio of $\Upsilon_{gm}^{(top)}$ with a top-hat window and $\Upsilon_{gm}^{(win)}$ with the lensing window as determined by the source and lens redshift distribution ($C_{integration} = \Upsilon_{gm}^{(top)}(r_p)/\Upsilon_{gm}^{(win)}(r_p)$). The “top” version is in the numerator because we construct E_G with the real lensing data, i.e., we implicitly computed and used the “win” version in the data. We want to divide that out and replace it with the “top” version when comparing with the theory. The lensing window can be written as follows:

$$W(\Pi) = \chi(z_m) - \chi(z_l) = \frac{1}{N} \int dz_l P_{lens}(z_l) \quad (19)$$

$$N = \int dz_l P_{lens}(z_l) \int_{z_m}^{\infty} dz_s P_{src}(z_s) \Sigma_{cr}^{-2}(z_l, z_s) \quad (20)$$

where the $\Sigma_{cr}(z_1, z_2)$ is given in Eq. (16). Currently our theory assumes that we simply take the galaxy matter cross-correlation ξ_{gm} , which is the correlation function between matter at that lens redshift and the lens galaxy position, and projected along the line of sight with a top-hat window. But in practice, if you have matter that is correlated with the lens but not exactly at the lens redshift, then the shear for that source is determined by $\Sigma_{cr}(z_m, z_s)$, which varies along the line of sight as z_m is closer to or farther away from the lens. The (z_l, z_m, z_s) are the redshifts of lens, matter and source

fect in practice (More et al. 2015), it is sufficient to describe the clustering signal observed in the data.

respectively. The innermost integral is to account for the fact that matter at z_m will lens all the sources behind matter ($z_s > z_m$) and $P_{src}(z_s)$ is the redshift distribution of source in our sample. The outer integral is to account for the fact that we have a distribution of lens given by $P_{lens}(z_l)$ which should be integrated over. The lens redshift sets the zero point of the line-of-sight separation (Π) for the galaxy-matter cross-correlation. Π is the comoving distance between matter and lens ($\Pi = \chi(z_m) - \chi(z_l)$). Here $\chi(z)$ is the comoving distance to the redshift z . We compute $W(\Pi)$ with the CFHTLenS source redshift distribution and CMASS lens redshift distribution. We use the N-body simulation to estimate the galaxy-matter cross-correlation and apply $W(\Pi)$ in order to compute the projected correlation function with the lensing window. Figure 5 shows the C_{win} correction we have computed for our sample. It is below 8% at the scales of interest.

6.3 Different redshift weighting of lensing and clustering

The weighting of the lensing signal averaged over redshift depends on the number of source galaxies behind a lens galaxy as a function of redshift. Within an annulus of fixed transverse separation, the galaxies at lower redshift have a higher number of sources behind them compared to galaxies at higher redshift. Also, clustering and lensing signal have different redshift weights. Specifically, our clustering measurement uses the weight w_{tot} defined by (12) for each galaxy, while the lensing measurement uses $w_{tot,l} \sum w_s \Sigma_{cr}^{ls-2}$ for each galaxy, where the summation runs over lens-source pairs for a given lens galaxy. This makes the effective redshift of the lensing measurement different from the effective redshift of clustering measurement. In order to correct for this difference in redshift, we compute the multiplication factor $C_z = \Upsilon_{gg}^{clust} / \Upsilon_{gg}^{lens}$. Here Υ_{gg}^{lens} is galaxy-galaxy clustering signal obtained with lensing weight as the function of redshift including both the annulus factor and the redshift weight and Υ_{gg}^{clust} is galaxy-galaxy clustering signal obtained without lensing weight. This shifts the effective redshift of the clustering signal to the effective redshift of lensing signal. Figure 5 shows the C_z correction we have computed for our sample. It is at the level of 2%.

6.4 Effects of Intrinsic Alignments

When photometric redshift errors cause galaxies that are at the lens redshift to be included in the source sample for the lensing measurement, the lensing measurement can be contaminated by intrinsic alignments (for reviews, see Troxel & Ishak 2015; Joachimi et al. 2015) of the false sources towards the lenses. The majority of the large-scale intrinsic alignment signal is carried by red galaxies (e.g., Hirata et al. 2007), for which the linear tidal alignment model (e.g., Hirata & Seljak 2004) provides a reasonable large-scale description that matches observations of this effect (e.g., Joachimi et al. 2011), and for which there are various descriptions on small scales (e.g., Blazek et al. 2015). In brief, pressure-supported galaxies form in primordial tidal fields due to large-scale structure; these tidal fields have stretching axes that point towards over-densities, and as a result the galaxies that form in those tidal fields also become radially aligned towards overdensities. This manifests as a negative galaxy-galaxy lensing signal, with intrinsically-aligned galaxies pointing radially towards the overdensities that our lens galaxies trace, reducing the measured Υ_{gm} . However, our removal of small-scale information partially mitigates the intrinsic alignment effect, which scales with separation

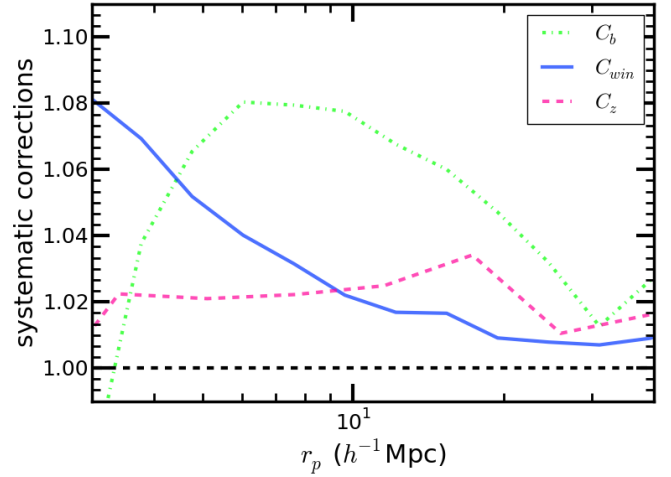


Figure 5. Figure shows the systematic corrections estimated for E_G . The green dashed-dotted line is the correction for the scale dependent bias (C_b ; see section 6.1). The blue solid line is for the correction due to difference in the clustering and lensing radial windows (C_{win} ; see section 6.2). The magenta dashed line is for the correction due to difference in redshift weighting of clustering and lensing (C_z ; see section 6.3).

roughly in the same way as the matter correlation function. Also, the photometric redshifts in CFHTLenS are good enough to reduce the contamination by physically-associated galaxies to a very low level, as demonstrated by the fact that we found a boost factor consistent with 1 to within 1.6 per cent at $r_p \gtrsim 1.5 h^{-1} \text{Mpc}$ (Section 4).

To estimate the magnitude of possible intrinsic alignment contamination in the galaxy-galaxy lensing signal in this work, we need several pieces of information. The first is the average intrinsic shear for galaxies that are within $\sim 100 h^{-1} \text{Mpc}$ of the CMASS galaxies in our source sample. To estimate this, we use the average intrinsic shear of LOWZ galaxies as a function of r_p , from Singh et al. (2015). We then use the redshift evolution of the linear alignment model to decrease this by a factor of 0.85 to go to the CMASS redshift (Hirata & Seljak 2004), and by a factor of ten to account for the fact that the sources that are used here are on average about eight times fainter than LOWZ galaxies. The factor of ten arises because intrinsic alignments are consistent with a slightly steeper than linear scaling with luminosity for red galaxies, as determined empirically in Joachimi et al. 2011 and Singh et al. 2015, though this is an extrapolation below the luminosity range in which their measurements exist. This gives an estimate of $\langle \gamma_{int} \rangle$ for the source sample used in this work.

In cases where there are many satellite galaxies at the lens redshift included in the “source” sample, and thus a boost factor substantially in excess of 1, it is common practice to assume that only those excess galaxies are intrinsically aligned (e.g., Blazek et al. 2012). In our case, there are essentially no “excess” galaxies, but we still must assume that non-excess galaxies near the lenses are intrinsically aligned. To account for this, we calculate the fraction of sources that are within $100 h^{-1} \text{Mpc}$ along the line-of-sight from a typical CMASS galaxy, given the source $p(z)$. For example, for a fixed redshift z_{lens} ,

$$f_{local}(z_{lens}) = \int_{z_{lower}}^{z_{upper}} dz p(z) \quad (21)$$

where the lower and upper limits of integration are defined by finding the redshift corresponding to $\pm 100h^{-1}\text{Mpc}$ separations from the lens redshift, and we assume the source $p(z)$ are normalized to integrate to unity over all redshifts. We average the $f_{\text{local}}(z_{\text{lens}})$ estimates over the lens redshift distribution. This average fraction $\langle f_{\text{local}} \rangle$ is approximately 0.05. Finally, we compare $\langle \gamma_{\text{int}} \rangle \langle f_{\text{local}} \rangle$, which is the total estimated intrinsic alignments contamination to the shear, with the measured shear. The estimated contamination has a maximum value (as a function of r_p) of 1 per cent of the measured shear, or at most 0.1σ . Even if some of the above assumptions are incorrect by a factor of two, we conclude that we can safely ignore intrinsic alignment contamination in our measurement, particularly given that (a) the estimates from Singh et al. (2015) were for red galaxies, and many of the sources are blue galaxies; and (b) the redshift-dependent lens-weighting will suppress the contributions from these more “local” galaxies that may be intrinsically aligned.

6.5 Fingers of God in RSD β

Galaxies that are satellites orbiting within the same halo exhibit random motions due to the gravitational potential well of the halo. This can cause galaxies at the same line of sight distance to have different redshifts, so that they appear to be spread out into a very elongated structure along the line of sight. This effect is known as fingers of god. We have modeled the fingers of god by introducing a parameter σ_{FOG} , a scale-independent additive term in the velocity dispersion of the Gaussian Streaming Model (GSM) (Reid & White 2011). Alam et al. (2015b) shows that this model recovers the expected parameter for the PTHalo mocks (Manera et al. 2013) and N -body mocks (Tinker et al. (2016), in prep.). This means that our fingers of god modeling is accurate enough for the scales used in our redshift space distortion analysis. The expected bias in the measurement of f should be below 2.6%, much smaller than the uncertainty in other measurements, as shown in Figure 6. We do not expect any extra bias in our E_G measurement from β .

6.6 Cosmic Variance

The CFHTLenS is a relatively small area of sky covering 170 square degree. The overlap between CFHTLenS and BOSS is 105 square degrees. This raises the question of our lensing measurement being limited by cosmic variance. We have estimated the cosmic variance from simulations by dividing our N -body simulation into roughly 105 square degree regions at $z = 0.57$. The CFHTLenS survey consists of four fields W1–W4 with overlapping areas of 48, 3, 33, and 21 square degrees with the CMASS DR11 sample respectively. The areas of each of the four fields are equivalent to areas of squares of side length 176, 44, 146 and 116 $h^{-1}\text{Mpc}$ at redshift $z = 0.57$. We tried to mimic this in our simulations by having four square with equivalent areas separated by 100 $h^{-1}\text{Mpc}$ from each other. Also, we limit our galaxies in the simulations along the z axis within 600 $h^{-1}\text{Mpc}$ in order to have a line-of-sight extent equivalent to CMASS sample between redshift of 0.43 and 0.7. However, matter particles are used for the full extent of the periodic box along z axis to account for the broad extent of the lensing kernel. We created 89 such realizations and computed Υ_{gm} for each realization. The variance of Υ_{gm} from these 89 realizations should give us an estimate of cosmic variance in our analysis. We have found that the cosmic variance is comparable to the lensing statistical error due to shape noise. We have also looked at the effect of changing the distance between our four

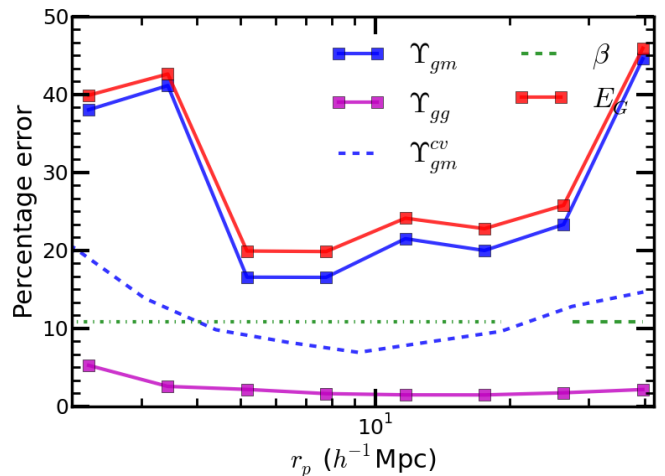


Figure 6. Figure shows the percentage error in different components of our measurement. The magenta line shows the error in Υ_{gg} , which is the lowest. The blue line represents the lensing error, and the dashed blue line is an estimate of the cosmic variance due to the finite size of the CFHTLenS fields. The green line is the error on the measurement of the RSD parameter β , and the red line is the combined error on our measurement of E_G . Note that β is measured only above 26 $h^{-1}\text{Mpc}$, shown with a dashed line.

sub-fields and found no significant affect in our estimate of cosmic variance. Figure 6 shows the percentage error in different component of our measurement. The dashed blue line in the figure represents cosmic variance on Υ_{gm} . We believe that our cosmic variance estimates are underestimated in the largest bins by not incorporating the actual shapes of the CFHTLenS subfields in our simulation, which can reduce the number of large scale modes available and hence increase the error in the largest bins. We estimate error on our lensing measurement using two methods described in section 4.2 and shown in Figure 1. We found that the difference between the covariance estimated from MD-Patchy mocks and using a combination of randoms with cosmic variance is within 3 per cent at $r_p \lesssim 30h^{-1}\text{Mpc}$. We use the error estimates from MD-Patchy in our final results.

6.7 Calibration Bias

Biases in the estimation of the ensemble lensing shear from the shape measurements of galaxies are one of the major systematics in galaxy lensing measurements. The inaccurate modeling of galaxy shape and PSF could leave both isotropic and anisotropic residuals in the ensemble shear. These residuals affect our shear measurements and can be parametrized as multiplicative and additive corrections (Heymans et al. 2006). The shape catalogue of CFHTLenS used in our analysis is corrected for these effects as described in Miller et al. (2013). We have also shown that our HOD tuned to match galaxy clustering also matches the lensing measurements without any tuning (see Figs. 2 and 4), indicating the absence of any statistically significant calibration bias. Although this is not a perfect test, as differences in cosmological parameters such as Ω_m between simulation and reality could potentially absorb such a bias. Note that Liu et al. (2016) shows that a multiplicative bias could be detected in the faint subset of the CFHTLenS sample, but this could also be absorbed in many other unknowns and not necessarily hint towards a need for multiplicative bias correction.

Another possible systematic uncertainty in the lensing measurements is due to the bias in the photo- z estimates. In Miyatake et al. (2015), they confirmed that the shift of the lensing signal is within a few percent for the possible range of the photo- z bias $\delta z = \pm 0.02$ (Erben et al. 2013), which is well below the statistical uncertainty in our lensing measurements.

6.8 Impact of R_0

The Υ used in the measurement of E_G attempts to remove the information from scales below R_0 and makes the measurement insensitive to our lack of understanding of small scale physics. In principle, there are many unknowns at scales below the virial radius, which are sensitive to baryonic physics, feedback models, stochasticity and other details related to galaxy formation. Also, the simulation used in our study lacks all of the above mentioned details and is obtained by populating N -body halo catalog using HOD model. This lack of details leads to failure in the description of the clustering and E_G measurement at the smallest scales. It is important to note that the choice of R_0 affects the measurement of E_G above R_0 by changing the scale dependence of the bias. We remove the impact of R_0 from larger scales by applying a correction factor C_b (see section 6.1 for details). Therefore measurements of E_G will be insensitive to R_0 as long as it is large enough to remove scales which we do not model in our simulations and corrections. Hence the choice of R_0 should be based on the minimum scales that our simulations can model for the observed clustering and lensing signal within error. We have found that our simulations can model the clustering and lensing signal down to scales $1.49h^{-1}\text{Mpc}$ (see Figure 2 and 4). Therefore, we used $R_0 = 1.49h^{-1}\text{Mpc}$ in this paper. Note that a higher value of R_0 will also degrade the signal to noise ratio of our final measurement. Hence one should minimize the value of R_0 .

We have also investigated the correction factor C_b when we use the extreme case of $R_0 = 0$. This will imply using $\Delta\Sigma$ in place of Υ for the measurement of E_G . In order to compute the correction factor for such a scenario, we need to predict the clustering signal down to small scales beyond the capability of our simulations. Based on our HOD modeling we estimated that only 10% of CMASS galaxies are satellites. This means that the two-point correlation function at such small scales will be dominated by central-satellite pairs. If we assume that satellite galaxies sample NFW (halo density) profile, we can make a reasonable assumption that small scale clustering is given by the NFW profile. We obtained the maximum correction factor C_b to be 6% which is slightly smaller than the 8% correction obtained for Υ . So, we note that, if small scale clustering is modeled with NFW profile then the scale dependent correction factor C_b obtained using either $\Delta\Sigma$ or Υ are similar. We use Υ in the rest of the paper because this doesn't require any extra assumption about the nature of small scale clustering.

7 RESULTS

In this section we provide the details of our measurement of E_G and its covariance.

7.1 Measurement of $E_G(r_p)$

E_G is a combination of three different signals that is designed to be more sensitive to the modification of gravity. We have measured

$\Upsilon_{gg}(r_p)$ and $\Upsilon_{gm}(r_p)$ for $2.28 < r_p < 40h^{-1}\text{Mpc}$ in 8 logarithmic bins as described in Section 4. We combine our measured signal to get $E_G(r_p)$ as in Eq. (1), then multiply by $C_b C_{win} C_z$ as in Sec. 6 in order to correct for differences in how Υ_{gg} and Υ_{gm} are measured that result in deviation from theoretical predictions. Figure 7 shows our measurement of $E_G(r_p)$. The blue (red) points show the measurement before (after) systematic corrections. The black line shows the GR prediction and the shaded region is one sigma error according to Planck (2015; TT+lowP+lensing; Planck Collaboration et al. 2014b).

7.2 Covariance matrix of E_G

The covariance of Υ_{gm} has been computed as described in Section 4. The covariance on Υ_{gg} is obtained using jackknife. The error on measurement of β was obtained as part of the redshift space distortion analysis described in Alam et al. (2015b). We compute the diagonal error on E_G by adding the errors from Υ_{gm} , Υ_{gg} and β in quadrature as

$$\sigma_{E_G}(r_p) = E_G(r_p) \sqrt{\left(\frac{\sigma_{\Upsilon_{gm}}}{\Upsilon_{gm}}\right)^2 + \left(\frac{\sigma_{\Upsilon_{gg}}}{\Upsilon_{gg}}\right)^2 + \left(\frac{\sigma_{\beta}}{\beta}\right)^2} \quad (22)$$

The above equation also assumes that the signal-to-noise ratio of all quantities is high enough that the error distribution on the ratio is a Gaussian. This is a good assumption because the signal in each bin is detected at the 5σ level or better. We then compute the correlation matrix of Υ_{gm} given by

$$\Psi_{gm}(r_i, r_j) = \Sigma_{gm}(r_i, r_j) / \sqrt{(\Sigma_{gm}(r_i, r_i) \Sigma_{gm}(r_j, r_j))} \quad (23)$$

where $\Sigma_{gm}(r_i, r_j)$ represents the covariance matrix of Υ_{gm} . The covariance matrix for E_G is obtained by multiplying the σ_{E_G} with the correlation matrix,

$$\Sigma_{E_G}(r_i, r_j) = \sigma_{E_G}(r_i) \sigma_{E_G}(r_j) \Psi(r_i, r_j) \quad (24)$$

Figure 8 shows the correlation matrix of E_G we have measured. We have assumed that the different components of E_G are independent while estimating the covariance matrix. It is a reasonable assumption because the clustering signal Υ_{gg} and lensing signal Υ_{gm} are integrated along the line of sight and hence will not be correlated with the redshift space distortions parameter β . Also, the lensing measurement is dominated by shape noise with errors at the 20% level on all scales, whereas the statistical errors on the clustering measurements are below 5% at all scales. Moreover the lensing is measured in a very small fraction of the area used for the clustering measurement. For both reasons, the clustering and lensing are independent in our analysis, justifying the use of the Υ_{gm} correlation matrix to estimate the covariance matrix for E_G .

7.3 Constraint on E_G

We have shown our measurement of E_G in logarithmic bins of r_p in Figure 7. We can obtain a measurement of E_G at an effective average scale by combining the information from all scales. The constant E_G model can be used in order to obtain the constraint on E_G using our measurement. We have used measurements between r_p of $5.17h^{-1}\text{Mpc}$ and $26.4h^{-1}\text{Mpc}$. The lower limit is to avoid small scales where systematic corrections become large and baryonic physics might start to become important (Mohammed et al. 2014). The upper limit is determined by the scale at which the systematic correction for the lensing becomes substantial compared to

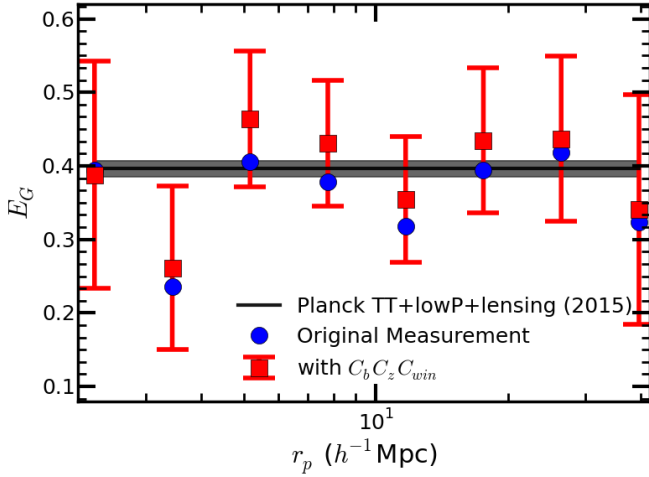


Figure 7. The plot shows E_G as a function of r_p . The blue points show the raw measurement (without any corrections) and the red points are the final measurement after multiplying by systematic corrections ($C_b C_z C_{win}$). The black line is the prediction of GR for Planck (2015; TT+lowP+lensing) cosmology with shaded region representing 1σ error.

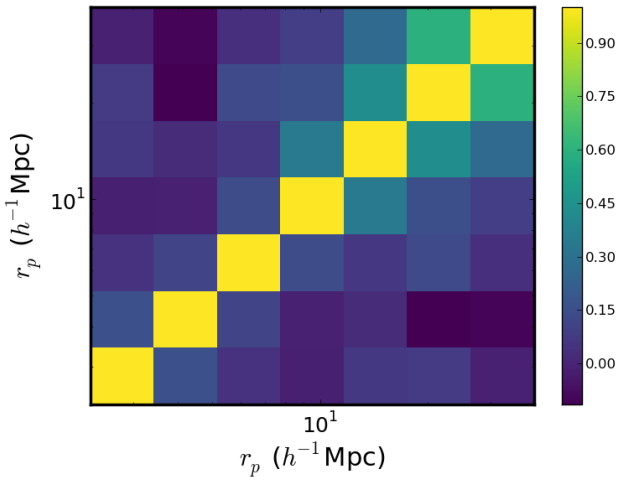


Figure 8. Correlation matrix (Ψ) of E_G : We have estimated the covariance of Υ_{gm} using 150 MD-Patchy mocks. This covariance is then used to compute the correlation matrix (see Eq. 23 for details).

the lensing signal itself. We fit our measurements of $E_G(r_p)$ with the full covariance matrix using the model of constant E_G , giving $E_G(z = 0.57) = 0.42 \pm 0.056$. Figure 9 shows our likelihood for E_G as a red solid line. The black line and the shaded region are the Planck (2015; TT+lowP+lensing) prediction. The magenta dashed line is the measurement of Blake et al. (2016). Our measurement is consistent with the Planck prediction and agrees with Blake et al. (2016). Our final measurement of E_G has an 13% statistical uncertainty, which is 30% improvement on the previous best measurement at the same redshift (Blake et al. 2016). Note that the Blake et al. (2016) measurement is 1.4σ from the Planck 2015 cosmology but less than 1σ from the WMAP7 cosmology, which is closer to their assumed cosmology.

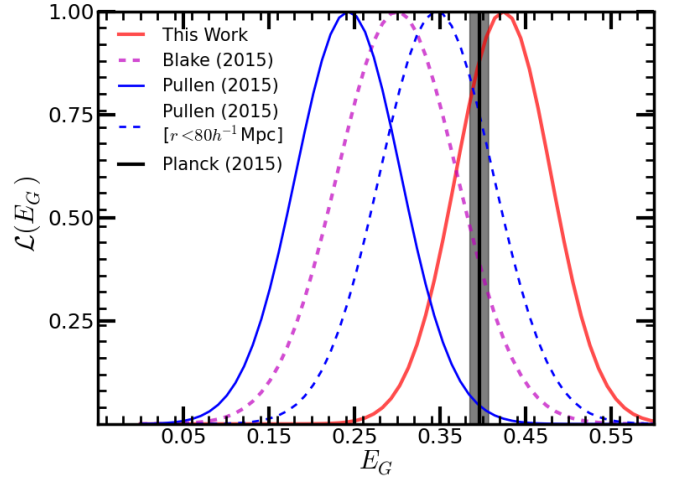


Figure 9. Figure shows the one-dimensional likelihood of E_G . The red solid line shows our measurement $E_G = 0.42 \pm 0.056$. The magenta dashed line is the measurement reported in Blake et al. (2016), $E_G = 0.30 \pm 0.07$. The blue solid and dashed lines are measurement from Pullen et al. (2016) using all scales ($E_G = 0.243 \pm 0.061$) and scales below $80 h^{-1} \text{Mpc}$ ($E_G = 0.346 \pm 0.066$) respectively. The black shaded region is the GR prediction for Planck (2015; TT+lowP+lensing). Note that Blake et al. (2016) assumes a cosmology with $\Omega_m = 0.27$ whereas we use the Planck 2015 cosmology.

8 DISCUSSION

We have analyzed data from CFHTLenS (Heymans et al. 2012) and the SDSS-III BOSS DR11 CMASS sample (Alam et al. 2015a). We have measured tangential shear by cross-correlating the CFHTLenS galaxy shapes with the lens sample (CMASS). This produces a measure of the excess surface mass density $\Delta\Sigma$. We have also measured redshift space galaxy-galaxy clustering ($w_p(r_p)$) and the redshift space distortions parameters (β). All of these measurements are tested for various systematics as described in Section 4. We then cast these measurements in terms of the annular differential surface densities (ADSDs; Baldauf et al. 2010) to suppress the small scale information. The Υ_{gg} is defined to match the kernel with Υ_{gm} . These measurements are then combined to estimate $E_G(r_p)$ (see Figure 7). We have also estimated the covariance on our measurements by combining the covariance of Υ_{gm} with the diagonal error on Υ_{gg} and β in quadrature (see Figure 8). The scale-averaged measurement of E_G is obtained by fitting a constant E_G model. We have also considered potential systematic errors that can affect our measurements of E_G and computed possible corrections or provided upper limits (see Section 6). We finally report $E_G(z = 0.57) = 0.42 \pm 0.056$ (13% error) compared to the ΛCDM prediction of $E_G = 0.40$ using the Planck Collaboration et al. (2014a) cosmology.

Our measurements are completely consistent with the prediction of ΛCDM , and provide a non-trivial test of GR at cosmological scales by virtue of probing both metric potentials. The first measurement of E_G , reported in Reyes et al. (2010) at redshift of 0.32, was also consistent with ΛCDM . A more recent measurement was reported in Blake et al. (2016) at redshifts 0.32 and 0.57. We improve on the measurement of Blake et al. (2016) by about 30% in precision at redshift of 0.57. This improvement largely comes from the fact that we are using the BOSS DR11 sample, which has more data compared to the BOSS DR10 sample used by Blake

et al. (2016), and from the improved precision on β measurement, which we obtained using a different perturbation theory template. A similar measurement was first proposed in Pullen et al. (2015) and measured in Pullen et al. (2016) by replacing the gravitational lensing shear estimated using galaxies with CMB lensing. This is a complimentary measurement to ours by virtue of probing different scales with different systematics. Pullen et al. (2016) reported $E_G = 0.243 \pm 0.061$ using scales upto $150h^{-1}\text{Mpc}$ and $E_G = 0.346 \pm 0.066$ using scales upto $80h^{-1}\text{Mpc}$. Our measurement is consistent with the measurement of E_G using CMB lensing at small scales ($r < 80h^{-1}\text{Mpc}$). But it shows 2.8σ tension when compared with their final results, which include large scales. This might indicate that these measurements have reached a limit where observational systematics are approaching the statistical uncertainty, and future surveys will require improved analysis methods.

We are entering the golden age of precision cosmology with much bigger and deeper surveys. For example, we have HSC, KIDS and DES taking data now, and LSST, WFIRST and Euclid happening in the next decade. The next generation surveys will provide an unprecedented handle on statistical errors, which necessitates a much better understanding of systematic errors. Using future surveys, we will be able to measure E_G much more precisely at multiple redshifts and over a wide range of scales. Such measurements will enable us to test the predictions of the ΛCDM model of structure formation as a function of scale and time, which might provide key insights into dark energy, dark matter, and the theory of gravity.

ACKNOWLEDGMENTS

We would like to thank Sukhdeep Singh for many insightful discussion during the course of this project. We would also like to thank anonymous referee for useful comments. SA and SH are supported by NASA grants 12-EUCLID11-0004 and NSF AST1412966 for this work. SH is also supported by DOE and NSF AST1517593. HM acknowledges the support of Japan Society for the Promotion of Science (JSPS) Research Fellowships for Young Scientists and the Jet Propulsion Laboratory, California Institute of Technology, under a contract with the National Aeronautics and Space Administration. RM acknowledges the support of the Department of Energy Early Career Award program.

SDSS-III is managed by the Astrophysical Research Consortium for the Participating Institutions of the SDSS-III Collaboration including the University of Arizona, the Brazilian Participation Group, Brookhaven National Laboratory, Carnegie Mellon University, University of Florida, the French Participation Group, the German Participation Group, Harvard University, the Instituto de Astrofísica de Canarias, the Michigan State/Notre Dame/JINA Participation Group, Johns Hopkins University, Lawrence Berkeley National Laboratory, Max Planck Institute for Astrophysics, Max Planck Institute for Extraterrestrial Physics, New Mexico State University, New York University, Ohio State University, Pennsylvania State University, University of Portsmouth, Princeton University, the Spanish Participation Group, University of Tokyo, University of Utah, Vanderbilt University, University of Virginia, University of Washington, and Yale University.

This work is based on observations obtained with MegaPrime/MegaCam, a joint project of CFHT and CEA/IRFU, at the Canada-France-Hawaii Telescope (CFHT) which is operated by the National Research Council (NRC) of Canada, the Institut National des Sciences de l'Univers of the Centre National de la

Recherche Scientifique (CNRS) of France, and the University of Hawaii. This research used the facilities of the Canadian Astronomy Data Centre operated by the National Research Council of Canada with the support of the Canadian Space Agency. CFHTLenS data processing was made possible thanks to significant computing support from the NSERC Research Tools and Instruments grant program.

REFERENCES

- Abazajian K. N., et al., 2009, *ApJS*, **182**, 543
- Ahn C. P., et al., 2012, *ApJS*, **203**, 21
- Aihara H., et al., 2011, *ApJS*, **193**, 29
- Alam S., et al., 2015a, *ApJS*, **219**, 12
- Alam S., Ho S., Vargas-Magaña M., Schneider D. P., 2015b, *MNRAS*, **453**, 1754
- Anderson E., 2010, preprint, ([arXiv:1009.2157](https://arxiv.org/abs/1009.2157))
- Anderson L., et al., 2014a, *MNRAS*, **439**, 83
- Anderson L., et al., 2014b, *MNRAS*, **441**, 24
- Bagla J. S., 2002, *Journal of Astrophysics and Astronomy*, **23**, 185
- Baldauf T., Smith R. E., Seljak U., Mandelbaum R., 2010, *Phys. Rev. D*, **81**, 063531
- Bartelmann M., Schneider P., 2001, *Phys. Rep.*, **340**, 291
- Bennett C. L., et al., 2013, *ApJS*, **208**, 20
- Benson A. J., Cole S., Frenk C. S., Baugh C. M., Lacey C. G., 2000, *MNRAS*, **311**, 793
- Berlind A. A., Weinberg D. H., 2002, *ApJ*, **575**, 587
- Beutler F., et al., 2012, *MNRAS*, **423**, 3430
- Beutler F., et al., 2014, *MNRAS*, **443**, 1065
- Blake C., et al., 2011, *MNRAS*, **418**, 1707
- Blake C., et al., 2016, *MNRAS*, **456**, 2806
- Blanton M. R., Lin H., Lupton R. H., Maley F. M., Young N., Zehavi I., Loveday J., 2003, *AJ*, **125**, 2276
- Blazek J., Mandelbaum R., Seljak U., Nakajima R., 2012, *J. Cosmology Astropart. Phys.*, **5**, 041
- Blazek J., Vlah Z., Seljak U., 2015, *J. Cosmology Astropart. Phys.*, **8**, 015
- Bolton A. S., et al., 2012, *AJ*, **144**, 144
- Cacciato M., van den Bosch F. C., More S., Mo H., Yang X., 2013, *MNRAS*, **430**, 767
- Carlson J., Reid B., White M., 2013, *MNRAS*, **429**, 1674
- Chuang C.-H., et al., 2016, *MNRAS*, **461**, 3781
- Cole S., et al., 2005, *MNRAS*, **362**, 505
- Cooray A., Sheth R., 2002, *Phys. Rep.*, **372**, 1
- Dawson K. S., et al., 2013, *AJ*, **145**, 10
- Doi M., et al., 2010, *AJ*, **139**, 1628
- Einstein A., 1915, Sitzungsberichte der Preussischen Akademie der Wissenschaften zu Berlin, pp 844–847
- Einstein A., 1916, *Annalen der Physik*, **49**, 770
- Eisenstein D. J., et al., 2005, *ApJ*, **633**, 560
- Eisenstein D. J., et al., 2011, *AJ*, **142**, 72
- Erben T., et al., 2013, *MNRAS*, **433**, 2545
- Feldman H. A., Kaiser N., Peacock J. A., 1994, *ApJ*, **426**, 23
- Fukugita M., Ichikawa T., Gunn J. E., Doi M., Shimasaku K., Schneider D. P., 1996, *AJ*, **111**, 1748
- Gunn J. E., et al., 1998, *AJ*, **116**, 3040
- Gunn J. E., et al., 2006, *AJ*, **131**, 2332
- Guo H., Zehavi I., Zheng Z., 2012, *ApJ*, **756**, 127
- Hamilton A. J. S., 1992, *ApJ*, **385**, L5
- Han J., et al., 2015, *MNRAS*, **446**, 1356
- Heymans C., et al., 2006, *MNRAS*, **368**, 1323
- Heymans C., et al., 2012, *MNRAS*, **427**, 146
- Heymans C., et al., 2013, *MNRAS*, **432**, 2433
- Hildebrandt H., et al., 2012, *MNRAS*, **421**, 2355
- Hirata C. M., Seljak U., 2004, *Phys. Rev. D*, **70**, 063526
- Hirata C. M., Mandelbaum R., Ishak M., Seljak U., Nichol R., Pimbblet K. A., Ross N. P., Wake D., 2007, *MNRAS*, **381**, 1197

- Hoekstra H., Jain B., 2008, *Annual Review of Nuclear and Particle Science*, **58**, 99
- Hojjati A., Pogosian L., Zhao G.-B., 2011, *Journal of Cosmology and Astroparticle Physics*, **8**, 5
- Hudson M. J., et al., 2015, *MNRAS*, **447**, 298
- Hütsi G., 2006, *A&A*, **446**, 43
- Jee M. J., Tyson J. A., Schneider M. D., Wittman D., Schmidt S., Hilbert S., 2013, *ApJ*, **765**, 74
- Joachimi B., Mandelbaum R., Abdalla F. B., Bridle S. L., 2011, *A&A*, **527**, A26
- Joachimi B., et al., 2015, *Space Sci. Rev.*, **193**, 1
- Kahn F. D., Woltjer L., 1959, *ApJ*, **130**, 705
- Kaiser N., 1987, *MNRAS*, **227**, 1
- Kazin E. A., et al., 2010, *ApJ*, **710**, 1444
- Kitaura F.-S., et al., 2016, *MNRAS*, **456**, 4156
- Koyama K., 2006, *jcap*, **3**, 17
- Landy S. D., Szalay A. S., 1993, *ApJ*, **412**, 64
- Leauthaud A., et al., 2012, *ApJ*, **744**, 159
- Leonard C. D., Ferreira P. G., Heymans C., 2015, *J. Cosmology Astropart. Phys.*, **12**, 051
- Liu J., Ortiz-Vazquez A., Hill J. C., 2016, *Phys. Rev. D*, **93**, 103508
- Lupton R. H., Gunn J. E., Szalay A. S., 1999, *AJ*, **118**, 1406
- Mandelbaum R., et al., 2005, *MNRAS*, **361**, 1287
- Mandelbaum R., Slosar A., Baldauf T., Seljak U., Hirata C. M., Nakajima R., Reyes R., Smith R. E., 2013, *MNRAS*, **432**, 1544
- Manera M., et al., 2013, *MNRAS*, **428**, 1036
- Massey R., Kitching T., Richard J., 2010, *Reports on Progress in Physics*, **73**, 086901
- Miller L., et al., 2013, *MNRAS*, **429**, 2858
- Miyatake H., et al., 2015, *ApJ*, **806**, 1
- Mohammed I., Martizzi D., Teyssier R., Amara A., 2014, preprint, ([arXiv:1410.6826](https://arxiv.org/abs/1410.6826))
- More S., van den Bosch F. C., Cacciato M., More A., Mo H., Yang X., 2013, *MNRAS*, **430**, 747
- More S., Miyatake H., Mandelbaum R., Takada M., Spergel D. N., Brownstein J. R., Schneider D. P., 2015, *ApJ*, **806**, 2
- Padmanabhan N., et al., 2008, *ApJ*, **674**, 1217
- Peacock J. A., Smith R. E., 2000, *MNRAS*, **318**, 1144
- Percival W. J., et al., 2004, *MNRAS*, **353**, 1201
- Percival W. J., et al., 2010, *MNRAS*, **401**, 2148
- Perlmutter S., et al., 1999, *ApJ*, **517**, 565
- Pier J. R., Munn J. A., Hindsley R. B., Hennessy G. S., Kent S. M., Lupton R. H., Ivezić Ž., 2003, *AJ*, **125**, 1559
- Planck Collaboration et al., 2014a, *A&A*, **571**, A1
- Planck Collaboration et al., 2014b, *A&A*, **571**, A15
- Pullen A. R., Alam S., Ho S., 2015, *MNRAS*, **449**, 4326
- Pullen A. R., Alam S., He S., Ho S., 2016, *MNRAS*, **460**, 4098
- Refregier A., 2003, *ARA&A*, **41**, 645
- Reid B. A., White M., 2011, *MNRAS*, **417**, 1913
- Reid B. A., Seo H.-J., Leauthaud A., Tinker J. L., White M., 2014, *MNRAS*, **444**, 476
- Reid B., et al., 2016, *MNRAS*, **455**, 1553
- Reyes R., Mandelbaum R., Seljak U., Baldauf T., Gunn J. E., Lombriser L., Smith R. E., 2010, *Nature*, **464**, 256
- Riess A. G., et al., 1998, *AJ*, **116**, 1009
- Riess A. G., et al., 2011, *ApJ*, **730**, 119
- Ross A. J., et al., 2012, *MNRAS*, **424**, 564
- Rubin V. C., Ford Jr. W. K., 1970, *ApJ*, **159**, 379
- Saito S., Baldauf T., Vlah Z., Seljak U., Okumura T., McDonald P., 2014, *Phys. Rev. D*, **90**, 123522
- Sakstein J., 2015, preprint, ([arXiv:1502.04503](https://arxiv.org/abs/1502.04503))
- Sánchez A. G., et al., 2013, *MNRAS*, **433**, 1202
- Schneider P., 2005, ArXiv Astrophysics e-prints,
- Scoccimarro R., 2004, *Phys. Rev. D*, **70**, 083007
- Seljak U., 2000, *MNRAS*, **318**, 203
- Sheldon E. S., et al., 2004, *AJ*, **127**, 2544
- Singh S., Mandelbaum R., More S., 2015, *MNRAS*, **450**, 2195
- Smee S. A., et al., 2013, *AJ*, **146**, 32
- Smith J. A., Tucker D. L., Allam S. S., Jorgensen A. M., 2002, in American Astronomical Society Meeting Abstracts. p. #104.08
- Tinker J., Alam S., Ho S., 2016, xxxx, p. xx
- Troxel M. A., Ishak M., 2015, *Phys. Rep.*, **558**, 1
- Unruh W. G., 1993, ArXiv General Relativity and Quantum Cosmology e-prints,
- Velander M., et al., 2014, *MNRAS*, **437**, 2111
- Wang L., Reid B., White M., 2014, *MNRAS*, **437**, 588
- Weinberg D. H., Mortonson M. J., Eisenstein D. J., Hirata C., Riess A. G., Rozo E., 2013, *Phys. Rep.*, **530**, 87
- White M., Hernquist L., Springel V., 2001, *ApJ*, **550**, L129
- White M., Hernquist L., Springel V., 2002, *ApJ*, **579**, 16
- White M., et al., 2011, *ApJ*, **728**, 126
- York D. G., et al., 2000, *AJ*, **120**, 1579
- Zhang P., Liguori M., Bean R., Dodelson S., 2007, *Physical Review Letters*, **99**, 141302
- Zu Y., Mandelbaum R., 2015, *MNRAS*, **454**, 1161
- Zwicky F., 1937, *ApJ*, **86**, 217
- de la Torre S., et al., 2013, *A&A*, **557**, A54
- van den Bosch F. C., More S., Cacciato M., Mo H., Yang X., 2013, *MNRAS*, **430**, 725